Chapter 9
Applied Tribology in the Oil-Film Bearings

9.1 Introduction

Tribology is derived from the Greek word *tribos*, which means rubbing. It deals with the tribological phenomena, such as lubrication, friction, and wears in the moving parts. Thus, tribology becomes more and more important in automotive turbochargers in terms of synthetic lubricating oils, friction reduction, adhesion and abrasion friction, and wear reduction in the oil-film bearings including journal and thrust bearings.

9.2 Characteristics of Lubricating Oils

Lubricating oils used in the industrial and automotive applications are based on mineral and synthetic oils. The mineral oils are produced by refining crude oil containing long hydrocarbon chains of paraffin and aromatic hydrocarbon rings. On the contrary, the synthetic oils are manufactured by means of polymerizing olefin ethylene gained from cracking of petroleum to produce poly-alpha-olefins (PAOs) that have similar chemical properties of the paraffinic oils (mineral oils), but they could be used in the extreme conditions of high thermal and mechanical loads. There are two kind of synthetic oils, esters (chemical compounds like alcohols or phenols), and PAOs. Synthetic oils used in the automotive engines result from combining PAOs with about 15 % of a synthetic ester [4, 7]. Some high-end synthetic engine oils are sold under the commercial names, such as Castrol Edge, Castrol Magnatec (Castrol), Mobil 1-5W30, SHC 824, and SHC 629 (ExxonMobil).

Lubricating oils are generally classified into SAE viscosity grades (Society of Automotive Engineers) for the automotive applications and ISO grades (International Organization for Standardization) for the industrial applications. The

H. Nguyen-Schäfer, *Rotordynamics of Automotive Turbochargers*,
Springer Tracts in Mechanical Engineering, DOI 10.1007/978-3-319-17644-4_9

ISO viscosity grades (VG) are based on the average kinematic viscosity in Centistokes at 40 °C oil temperature.

The kinematic viscosity is defined as the ratio of the dynamic viscosity to density.

$$\nu = \frac{\eta}{\rho} \tag{9.1}$$

where

ν is the kinematic viscosity [m^2/s; mm^2/s; 1 cSt (Centistokes) = 1 mm^2/s];
η is the dynamic viscosity [Ns/m^2; Pa s; 1 cP (Centipoise) = 1 mPa s];
ρ is the oil density [kg/m^3; g/mm^3].

The SAE grade has a general form SAE xWy (e.g., SAE 5W30), where xW stands for the oil viscosity grade of SAE xW (SAE 5W); W stands for winter at −18 °C (0 °F) for low temperature applications. The index y relates to the oil viscosity grade SAE y (i.e. SAE 30) at about 100 °C (212 °F) for high temperature applications.

Table 9.1 gives the equivalent lubricating oils between the ISO VG (Viscosity Grade) and SAE specifications and their HTHS viscosities according to SAE J300. The lubricating oil of SAE 5W30 corresponds to ISO VG 22 for SAE 5W in low temperatures and ISO VG 100 for SAE 30 in high temperatures with a HTHS viscosity of 2.9 mPa s at 150 °C (302 °F) and oil share rate of 10^6 s^{-1}.

In fact, oil viscosities change almost with temperature at small or moderate oil shear rate. Generally, the higher the oil temperature is, the lower the oil viscosity becomes, and vice versa. The oil dynamic viscosity versus temperature is calculated using the Cameron and Vogel equation, as given in Eq. (6.44a). Figure 9.1 gives the dynamic viscosities depending on oil temperatures for some common lubricating oils used in the industrial and automotive engines.

The related coefficients in the Cameron and Vogel equation in Eq. (6.44a) of common oils used in the automotive engines are given in Table 9.2. The coefficients

Table 9.1 Viscosity grades and HTHS viscosities of lubricating oils of the ISO and SAE specifications (SAE J300)

ISO VG grade	SAE grade	HTHS viscosity (mPa s)
–	0W	–
22	5W	–
32	10W	–
46	15W	–
68	20W/20	2.6
100	30	2.9
150	40	2.9[a]; 3.7[b]
220	50	3.7
320	60	3.7

[a] 0W40; 5W40; 10W40
[b] 15W40; 20W40; 25W40

Fig. 9.1 Dynamic viscosities of lubricating oils versus temperatures

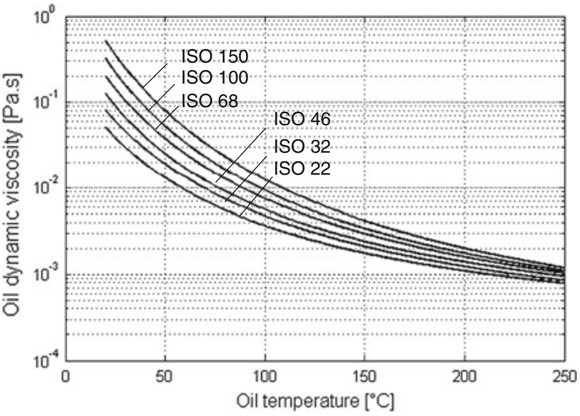

Table 9.2 Computed coefficients of oil dynamic viscosities

ISO VG grade	$\eta(T) = a\ \exp\left(\frac{b}{T(K)-c}\right)$		
	a (Pa s)	*b* (K)	c (K)
22	12.312e − 5	6.181e + 2	1.906e + 2
32	9.618e − 5	7.391e + 2	1.883e + 2
46	11.387e − 5	7.014e + 2	1.930e + 2
68	8.396e − 5	8.520e + 2	1.835e + 2
100	7.547e − 5	9.081e + 2	1.844e + 2
150	5.399e − 5	10.747e + 2	1.758e + 2

result from three points of the oil grade that are used to calculate of the dynamic viscosities η (Pa s) versus oil temperature T (K). The oil viscosities vary at each iteration step in the bearing dynamics and rotor dynamic computation.

9.3 HTHS Viscosity of Lubricating Oils

HTHS viscosity (high temperature high shear) is defined as the effective oil dynamic viscosity (mostly in mPa s) in the operating condition at the high oil temperature of 150 °C (302 °F) and large share rate of 10^6 s^{-1}.

The shear rate $\dot{\gamma}$ is the velocity gradient of the oil film that is defined as the change rate of the oil velocity to oil-film thickness.

$$\dot{\gamma} \equiv \left| \frac{\partial U}{\partial h} \right| \tag{9.2}$$

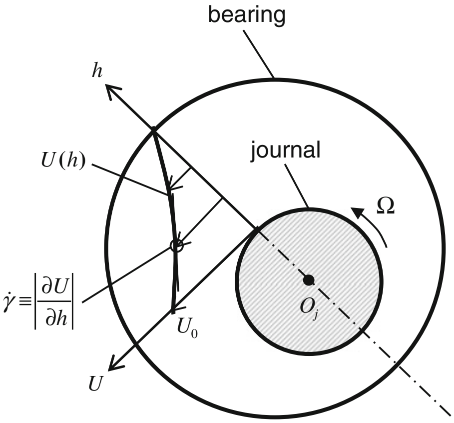

Fig. 9.2 Oil velocity profile and shear rate of the oil film

Figure 9.2 shows the velocity profile of the oil film in the bearing clearance of a fixed radial bearing with the journal circumferential velocity U_0. The shear stress τ of the oil film on the journal is proportional to the oil dynamic viscosity and shear rate.

$$\begin{aligned} \tau &= \frac{F_f}{A_S} = \eta \cdot \left|\frac{\partial U}{\partial h}\right| \\ &= \eta(T, \dot{\gamma}) \cdot \dot{\gamma} \equiv \tau(T, \dot{\gamma}) \end{aligned} \tag{9.3}$$

where F_f is the friction force acting on the journal; A_S is the oil-lubricated surface of the journal; T is the oil temperature.

In case of a Newtonian fluid, such as single-grade oils (base oils) the dynamic viscosity depends only on the fluid temperature and not on the shear rate, as shown in Fig. 9.3a. Hence, the shear stress is linear to the oil shear rate (see Fig. 9.4).

$$\tau = \eta(T) \cdot \dot{\gamma} \tag{9.4}$$

In fact, multi-grade lubricating oils are generally non-Newtonian fluids due to long hydrocarbon chains and aromatic rings. As a result, the oil dynamic viscosity depends on not only the oil temperature but on oil shear rate, as shown in Fig. 9.3b. Hence, the shear stress is a nonlinear function of the oil temperature and shear rate (see Fig. 9.4).

$$\tau = \tau(T, \dot{\gamma}) \tag{9.5}$$

Figure 9.3 shows the dynamic viscosity of a Newtonian fluid is independent of the shear rate at a constant temperature; it reduces only with oil temperatures. On the contrary, the oil viscosity (mostly non-Newtonian oils) is nearly constant as long as the shear rate is below the critical shear rate of 10^4 s^{-1} and strongly decreases with

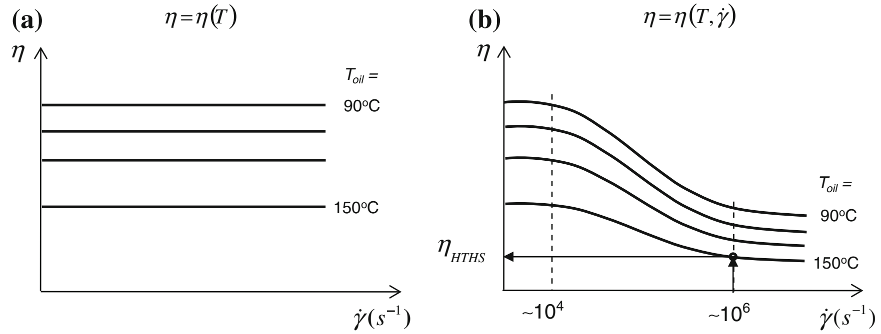

Fig. 9.3 Dynamic viscosity of lubricating oil versus shear rate and temperature shear rate. **a** Newtonian fluids. **b** Non-newtonian oils

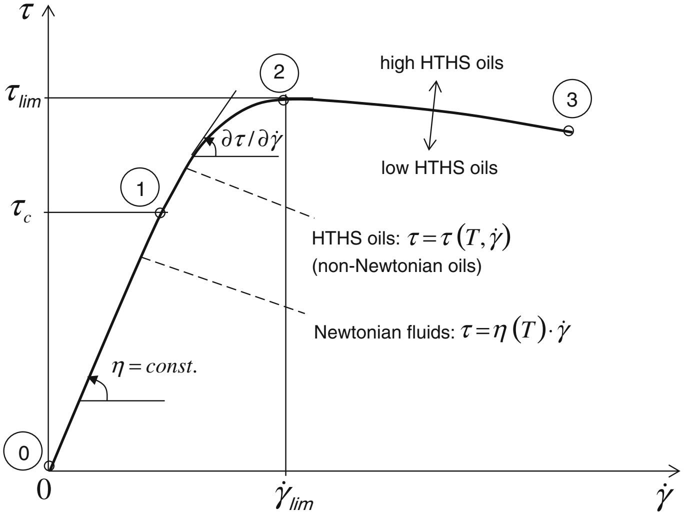

Fig. 9.4 Shear stress versus shear rate of lubricating oils

the oil shear rate up to 10^6 s^{-1}. From this shear rate, the oil viscosity remains unchanged at the lowest viscosity that is defined as the HTHS viscosity at the oil temperature of 150 °C. Generally, the oil shear rate in the bearing of the automotive turbochargers is very large due to their high rotor speeds in the small bearing clearances.

In the following section, the oil shear rate in the radial bearing of a typical turbocharger with a shaft diameter D = 7 mm supported on two rotating floating ring bearings (RFRBs) with a radial bearing clearance h = 10 μm is calculated.

Using Eq. (9.2), the shear rate of the oil film results in

$$\begin{aligned}\dot{\gamma} &\equiv \left|\frac{\partial U}{\partial h}\right| \approx \frac{U_{\mathrm{eff}}}{h}\\ &= \frac{(1-RSR)\,U_0}{h} = (1-RSR)\frac{\pi ND}{60h}\end{aligned} \tag{9.6}$$

where

U_{eff}	is the effective oil velocity in the RFRBs (m/s);
RSR	is the ring speed ratio (−) in Eq. (6.92);
D	is the shaft diameter (m);
N	is the rotor speed (rpm);
h	is the oil-film thickness (m).

According to Eq. (9.6), the oil shear rate is approximately $1.1 \times 10^6\ \mathrm{s}^{-1}$ at the rotor speed from 40,000 rpm with a ring speed ratio of 25 %. Additionally, the effective oil temperature in the bearing clearance is mostly at 150 °C or higher at high rotor speeds. Therefore, the oil viscosity almost in the operating conditions of turbochargers is the HTHS viscosity (see Fig. 9.3b).

There are three operating areas of the shear stress versus shear rate of lubricating oils: (0)–(1), (1)–(2), and (2)–(3), cf. Fig. 9.4.

(0)–(1): *Newtonian Fluids* ($\tau \le \tau_c$)

In this operating area, the lubricating oil is a Newtonian fluid (linear behavior) in which the oil viscosity only depends on the oil temperature and is independent of the shear rate. In case of constant temperature, the lubricant viscosity is unchanged until the shear stress reaches the critical stress τ_c. The shear stress is proportional to the shear rate with a constant viscosity η according to Eq. (9.4).

(1)–(2): *Non-newtonian Oils* ($\tau_c < \tau \le \tau_{lim}$)

At increasing the shear rate, the lubricant behaves like a non-Newtonian fluid (nonlinear behavior). In this operating area, the lubricant viscosity depends on both oil temperature and shear rate. As a result, the shear stress is a nonlinear function of oil temperature and shear rate (see Fig. 9.4). The result shows that the shear stress gradient is smaller than in case of the Newtonian fluid; i.e., the shear stress slowly increases with the shear rate. On the one hand, the higher the shear rate is, the lower the oil viscosity becomes, as shown in Fig. 9.3b. On the other hand, the shear stress increases with the shear rate. Both opposite effects are responsible for the nonlinear behavior of the shear stress versus shear rate.

(2)–(3): *Non-newtonian Oils* ($\tau > \tau_{lim}$)

As the shear rate exceeds the limit shear rate, the shear stress begins slowly decreasing with the shear rate from (2) to (3). At high shear rates, the oil temperature rises due to friction in the bearing leading to a fall of the oil viscosity. It reduces the shear stress more than the increasing shear stress due to raising the shear rate. As a result, the shear stress slightly decreases with the shear rate in this operating area.

In Fig. 9.4, the curve (0)–(1)–(2)–(3) moves upwards for high HTHS oils and moves downwards for low HTHS oils. It is obvious that the shear stress of high HTHS is larger than the lower HTHS oils at the same shear rate. Hence, the lower HTHS the lubricating oil is, the less the friction power is generated in the engine and turbocharger as well leading to less fuel consumption, higher fuel mileage miles per gallon (MPG), and reduction of NO_x and CO_2.

Lubricating oils are generally divided into two HTHS levels: low HTHS viscosity with $\eta_{HTHS} < 3.5$ mPa s and high HTHS viscosity with $\eta_{HTHS} \geq 3.5$ mPa s, as given in Table 9.1. The low HTHS oils with the HTHS viscosity between 2.9 and 3.5 mPa s generates less friction in the engine (i.e., higher mileage MPG, lower NO_x, CO_2 emissions), but more wears could occur in the moving parts, such as cylinders and pistons of the engine, bearings in the turbochargers, etc. Thus, the lifetime of the engine becomes shorter due to wears. On the contrary, the high HTHS oils with the HTHS viscosity larger than 3.5 mPa s cause more friction power in the engine (i.e., lower mileage MPG, higher NO_x, CO_2 emissions), but the moving parts are protected from wears. As a result, the long lifetime is warranted for the engine even at high thermal and mechanical operating conditions.

Therefore, the automotive industry must take the compromise between the low HTHS for high mileage MPG and low NO_x, CO_2 emissions and the high HTHS for the wear protection and the long lifetime of the engines to find out which HTHS value is appropriate for the engines. Recently, in order to reduce NO_x and CO_2 emissions according to the new emission law, some car manufacturers have been thinking of using an ultra-low HTHS oil of 2.6 mPa s, such as lubricating oil SAE 0W20. To overcome the problem of wears, the materials of moving parts must be improved such as coatings or new endurable materials. As a result, the car costs a little more. Eventually, customers have to pay the price increase for the environment protection. In turn, they could save money at the fuel consumption.

At operating conditions with the high rotor speeds, the effective HTHS oil viscosity reduces; therefore, the bearing stiffness and damping coefficients decrease. To keep the rotor in balance with the external forces, the induced pressure in the bearing clearance has to increase itself at reducing the oil-film thickness. Hence, the journal eccentricity ε increases under the load F in order to raise the bearing stiffness and damping coefficients. If the oil-film thickness is below the limit, as given in Fig. 6.11, the mixed or boundary lubrication (BL) takes place in the bearing clearance. Note that the more the bearing friction is, the smaller the oil film thickness becomes due to the high oil temperature. Finally, the oil film breaks up in the radial direction because the boundary contact occurs between the journal and bearing leading to seizure of the journal in the bearing (see Fig. 9.5). As a result, the HTHS viscosity has somehow to do with the shear instability of the oil-film that is to blame for break up of the oil-film in the bearing. At high rotor speeds, the higher the shear rate is, the lower the oil viscosity becomes and the thinner the oil-film thickness will be (see Fig. 9.3).

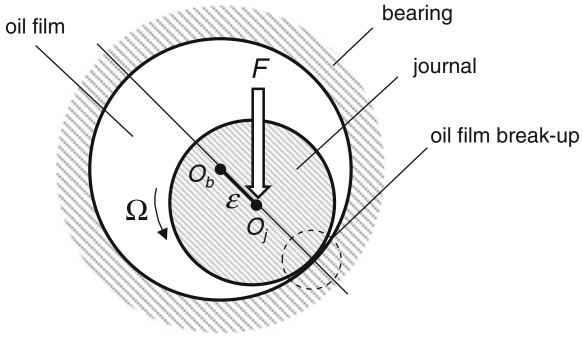

Fig. 9.5 Oil-film break up in the bearing clearance

9.4 Viscosity Index of Lubricating Oils

To prevent wear, VI improvers (polymeric additives) are added in lubricating oils in order to modify the viscosity change with oil temperature. They are based on the VI index. The viscosity index (VI) relates to the change rate of the oil temperature to its dynamic viscosity.

$$VI \propto \left| \frac{\partial T}{\partial \eta} \right| \tag{9.7}$$

According to Eq. (9.7), the smaller the viscosity changes with oil temperature, the higher the viscosity index VI is leading to the better oil quality. The viscosities of lubricating oils with the high and low VI versus oil temperatures are shown in Fig. 9.6. The viscosity of the high VI oil decreases with temperature more slowly compared to the viscosity of the low VI oil. That means the absolute viscosity gradient of the high VI oil is larger than the low VI oil. The higher the viscosity index VI is, the less the viscosity changes with oil temperature and vice versa. Obviously, the high VI oils are better for wear protection than the low VI oils at a large operating range of oil temperatures.

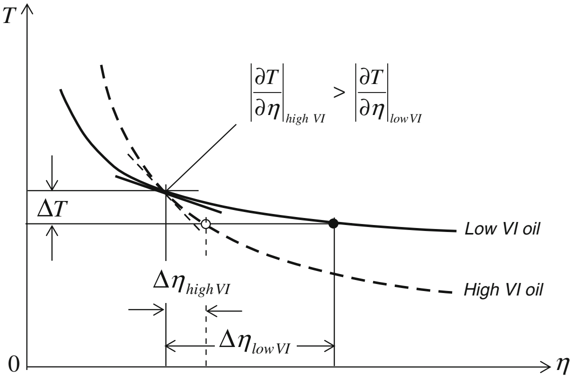

Fig. 9.6 Dynamic viscosity versus temperature of low and high VI oils

Synthetic oils (PAOs, esters) have mostly higher VI than the mineral oils because some chemical additives are added in the lubricants at the hydrocracking process. They have been produced and custom-tailored to optimize and simplify the molecular structures of the hydrocarbon chains and aromatic rings with predictably designed oil properties, instead of complex unpredictable molecular structures of the mineral oils with lower VI. As a result, synthetic lubricating oils are suitable for the extreme operating conditions with the high thermal and mechanical loads at high rotor speeds of automotive turbochargers.

Adding VI improvers (polymeric molecular additives) in the lubricating oils, the viscosity change with oil temperature reduces so that the HTHS effective viscosity is improved to prevent wears. The VI improvers regulate the oil viscosity with temperature in two ways. First, at low oil temperatures, the molecule chain contracts itself to generate more empty spaces for the oil molecules; therefore, the oil viscosity increases more slowly. Second, at high oil temperatures, the molecule chain expands itself to occupy more spaces in the oil molecules; hence, the oil viscosity reduces more slowly.

The viscosity index VI is a dimensionless number that is calculated by the ASTM D-2270 (American Society for Testing and Materials).

$$VI = 100 \times \left(\frac{L - U}{L - H} \right) \tag{9.8}$$

where

U is the viscosity of the test oil at 40 °C ($\sim$100 °F) in cSt;

L is the viscosity parameter at 40 °C of the first reference oil and is defined as

$$VI = 0 \; for \; L \; > H$$

H is the viscosity parameter at 40 °C of the second reference oil and is defined as

$$VI = 100$$

L and H are corresponding to the dynamic viscosity (cSt) of the test oil at 100 °C ($\sim$210 °F) are given in the ASTM D-2270;

To calculate the VI index, the oil viscosities at 40 and 100 °C are required. Their viscosity-related parameters L and H are given in the ASTM D-2270. The VI indexes of some commonly used lubricating oils are given in Table 9.3 [6].

Table 9.3 VI indexes of some automotive lubricating oils

Lubricating oils	Viscosity index (VI)
Mineral oils	80 … 120
Hydrocraking oils	125 … 150
Synthetic oils (PAOs)	140 … 160
Silicone oils (hydraulic fluids)	>200

9.5 Stribeck Curve

In the following section, the lubrication regions in the bearing clearance over the oil-film thickness are studied in the Stribeck curve. The oil-film thickness results from many rotordynamic and tribological influences, such as the acting force on the bearing, rotor speed, journal eccentricity, surface roughness, oil temperature, and as well as oil viscosity. If the current oil-film thickness is larger than the limit oil-film thickness, the friction in the bearing remains small; the bearing surface is protected from wear. In this case, the lubrication is fully hydrodynamic.

In order to look into the lubricating behaviors in the bearing, the dimensionless oil-film thickness λ is defined as the ratio of the minimum oil-film thickness to the root-mean-square (rms) combined surface roughness [1, 2, 4].

$$\lambda \equiv \frac{h_{\min}}{R_q} \tag{9.9}$$

where $h_{\min}$ is the minimum oil-film thickness, R_q is the rms combined surface roughness of the surfaces #1 and #2.

The rms-combined surface roughness is defined as

$$R_q \equiv \sqrt{R_{q1}^2 + R_{q2}^2} \tag{9.10}$$

within R_{q1} and R_{q2} are the rms roughness of the surfaces #1 and #2.

Using Gaussian distribution of the surface height, the rms roughness R_q is transformed into the arithmetic average roughness R_a by the factor of 1.25.

$$R_q = 1.25 R_a$$

Thus, the rms-combined surface roughness is written in the average roughness as

$$R_q = 1.25\sqrt{R_{a1}^2 + R_{a2}^2} \tag{9.11}$$

where R_{a1} and R_{a2} are the arithmetic average roughness of the surfaces #1 and #2.

The lubrication regions in the Stribeck curve are classified into four lubrication regions according to [4]:

- $\lambda \le 1$: boundary lubrication (BL)
- $1 < \lambda \le 5$: partial boundary lubrication (PBL)
- $3 < \lambda < 10$: mixed lubrication (ML) containing elasto-hydrodynamic lubrication (EHL: $5 \le \lambda \le 8$)
- $\lambda \ge 10$: fully hydrodynamic lubrication (HL: $\lambda \ge 8$–10)

In case of $\lambda \le 1$, the BL occurs between the surfaces in which the oil-film thickness is very small in the order of a few nanometers (10^{-9} m). In this oil film thickness, the molecules of hydrocarbon chains of the lubricating oil or polymer additives keep the moving surfaces separate from each other in the nanotribology consideration. Due to the very narrow oil film thickness, the friction coefficient strongly increases leading to seizure of materials between the moving surfaces under heavy loads.

As the dimensionless film thickness λ increases from 1 to 5, the partial BL occurs in which the surfaces partially contact each other between the BL (in the nanotribology $\sim 10^{-9}$ m) and ML (in the microtribology $\sim 10^{-6}$ m). The nanotribology is generally used to explain the tribological effects in the microtribology. At first, the friction coefficient remains nearly constant in the BL and then slightly decreases with the oil-film thickness in the ML. However, the friction coefficient is still high since the abrasive and adhesive frictions occur between the moving surfaces in the mixed BL.

The EHL occurs in the ML at $5 \le \lambda \le 8$, in which the asperities between the surfaces have been plastically deformed or removed due to abrasive and adhesive wears. As soon as the asperities of the surfaces disappear or do not touch with each other at increasing oil-film thickness, the friction coefficient drops significantly to the minimum where the fully HL begins (see Fig. 9.7).

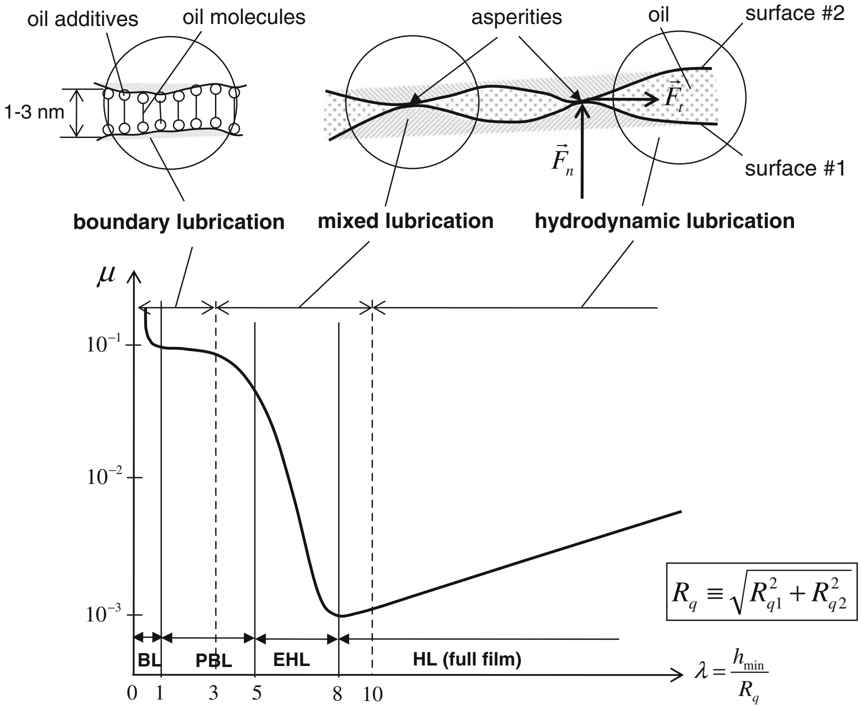

Fig. 9.7 Lubrication regions in the Stribeck curve μ-λ

In case of $\lambda \geq 10$, the moving surfaces are fully separated by the large oil-film thickness without contact of any asperity at less abrasive and adhesive frictions. This lubrication regime is called fully HL. The friction induced in this region is only the viscous friction of the oil film.

The friction coefficient in the fully HL is calculated as [9]

$$\mu_{\mathrm{HL}} = \frac{F_t}{F_n} \propto \frac{(1/h)}{1/h^2} = h \propto \lambda \tag{9.12}$$

where

h is the current minimum oil-film thickness;
λ is the dimensionless oil-film thickness;
F_t is the friction force proportional to inversely related to the film thickness ($1/h$);
F_n is the normal force proportional to $1/h^2$.

According to Eq. (9.12), the friction coefficient is proportional to the dimensionless oil-film thickness in the fully HL.

In the partial boundary or ML regions, the oil temperature in the bearing clearance is relatively high due to the large bearing friction. When the effective oil temperature in the bearing exceeds the flash points of the lubricating oil 210 °C (SAE 5W30) and 250 °C (SAE 20W30) [6], the oil film begins coking inside the bearing clearance and leaves the hard coked-oil layer on the rotor shaft.

The process of oil coking generates a hard black thin layer of the carbonaceous residue on the surface of the journal within the bearing clearance. The hard coked-oil layer continually increases after a long operating time; hence, the radial bearing clearance reduces. As a result, the effective oil temperature further increases as the bearing clearance reduces, and the coking process continuously takes place. Finally, it causes seizure of the shaft in the bearing and fatal damage of turbochargers.

9.6 Surface Texture Parameters

Surface tribological characteristics play a key role in rotor stability and for wear in the bearings as well. They strongly affect the oil-film thickness that depends on the lubrication regime in the bearings (see Fig. 9.7). The oil film thickness involves the rotordynamic stability, induced airborne noises, and prevention of wear in the bearings. The oil-film bearings work on the hydrodynamic principle in which the inner oil film supports the rotor against the unbalance excitation forces and keep it stable during the operation. Moreover, the outer oil film provides the rotor with a large damping to keep it in small amplitudes at resonances and prevent the rotor from the oil whirl instability. Therefore, the outer oil film reduces the induced airborne noises, such as the unbalance whistle and constant tone. Without or poorly lubricated oil supply, the bearings cannot fulfill their functions in the turbocharger.

That could cause damage in the bearings and furthermore in the compressor and turbine wheels due to seizure of the wheels in their housings. The surface texture parameters are discussed in the following section.

9.6.1 Surface Height Profile

The surface roughness characteristics of the bearings, journal in the radial bearing, and thrust rings in the thrust bearing are tribological analyzed. The roughness profile of the surface is defined as the trace profile about the waviness profile of the surface (see Fig. 9.8).

At sampling the surface, the surface profile consisting of the waviness and roughness height profile is measured by a stylus and digitalized. The peak-to-peak amplitude of the waviness profile is defined as the waviness height W_t. The measured signal of the surface profile is amplified and analyzed by band-filter technique, as displayed in Fig. 9.9a. Using the high-pass filter, one obtains the surface roughness profile; and the surface waviness profile results from the low-pass filter. The waviness profile shows the plateau shape of the surface; the roughness height profile describes the real roughness height of the surface that is measured from the reference line. The roughness height profile is the arithmetic average value of the surface height in an evaluation length. The roughness profile contains many peaks (asperities) and valleys of the measured surface [8].

The mean value of the surface height is defined in the evaluation length l_n as

$$\begin{aligned} \bar{z} &\equiv \frac{1}{l_n}\int_0^{l_n} z(x)dx \\ &\approx \frac{1}{N}\sum_{i=1}^{N} z_i(x_i) \end{aligned} \tag{9.13}$$

where N is the sampling number of the surface height z_i measured from the reference line z_{ref} within the evaluation length l_n.

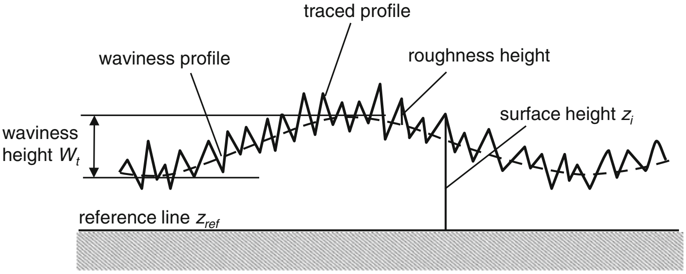

Fig. 9.8 Characteristics of the surface height profile

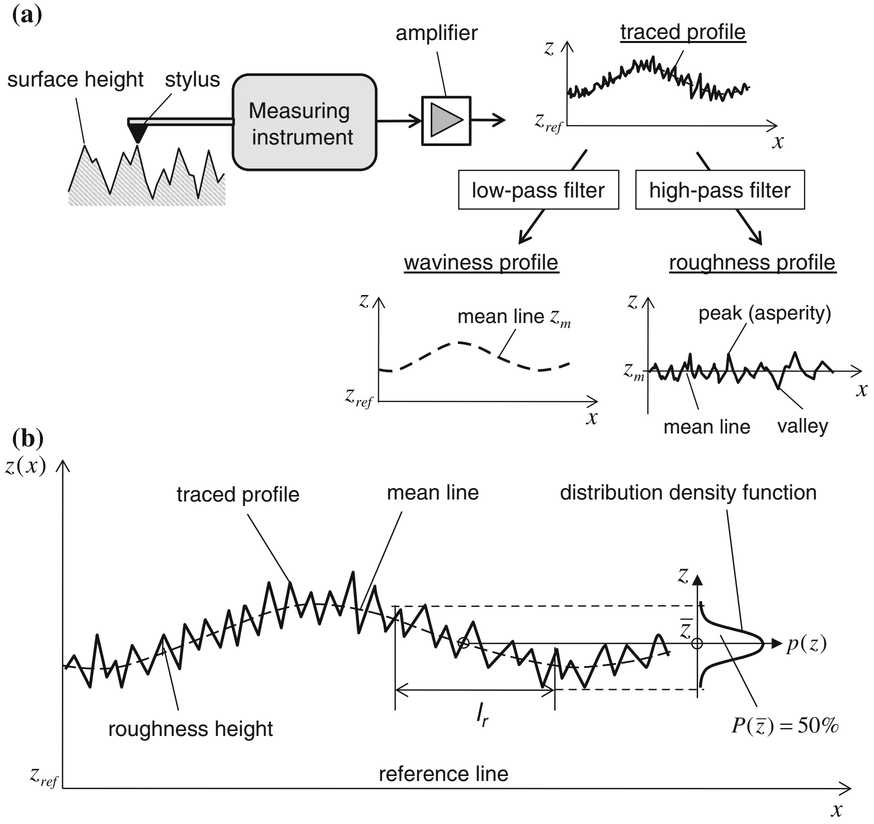

Fig. 9.9 **a** Analysis of the measured traced profile. **b** Distribution density function of the measured roughness height

In practice, the mean value of the surface height is determined by the Gaussian density function $p(z)$ within the sampling length l_r using the phase corrector filter. The mean value is the surface height value at the maximum density function whose probability function $P(z)$ equals 50 % (cf. Fig. 9.9b and Appendix D).

The variance s of the roughness height of N samplings in the sampling length l_r is calculated as

$$s \equiv \frac{1}{(N-1)} \sum_{i=1}^{N} (z_i - \bar{z})^2 \tag{9.14}$$

The standard deviation σ is defined as the square root of the variance s. It shows the variation of the measured values from the mean value of the surface roughness height in the normal distribution density function (see Appendix D). A small standard deviation indicates that the measured values tend to be close to the mean value; a large standard deviation shows that the measured values are spread out over a large range from the mean value.

Using Eq. (9.14), the standard deviation of N samplings in the sampling length l_r is written as

$$\sigma \equiv \sqrt{s} = \sqrt{\frac{1}{(N-1)} \sum_{i=1}^{N} (z_i - \bar{z})^2} \tag{9.15}$$

According to Appendix D, the smaller the standard deviation σ is, the better the production will be; e.g., a production with $\pm 3\sigma$ gives 99.7 % of its products that are within the given tolerances.

9.6.2 Surface Tribological Parameters

In the following section, we deal with some tribological parameters that are used to analyze the bearing surface roughness in the turbochargers [8].

- *Evaluation length* l_n is the length in which the values of the surface height are selected and evaluated. Its length is normally chosen by five times of the cutoff wavelength λ_c.

$$l_n \approx 5\lambda_c \tag{9.16}$$

- *Sampling length* l_r is the reference length for the roughness height evaluation and nearly equals the cutoff wavelength λ_c.

$$l_r \approx \lambda_c \tag{9.17}$$

- *Cutoff wavelength* λ_c is the profile filter that is used in analyzing the roughness height. It is generally chosen so that the amplitude of the roughness height with a sine function is reduced to about 50 % after filtering the measured signals. According to DIN EN ISO 4288:1998 and DIN EN ISO 3274:1998, some wavelengths are determined for profile filters as follows:

$$\lambda_c = 0.08;\ 0.25;\ 0.8;\ 2.5;\ 8.0\ \text{mm} \tag{9.18}$$

At decreasing the cutoff wavelength, the amplitude of the filtered surface roughness profile is also reduced; the amplitude of the filtered waviness profile of the surface roughness increases. Therefore, the short cutoff wavelength is rather preferred at small surface roughness of R_a and R_z.

- *Roughness* R_{sm} (DIN EN ISO 4287, ASME B46.1), see Fig. 9.10

It is called the *mean peak spacing* and defined by the arithmetic average value of five mean peak spacings of the roughness profile within the evaluation length l_n.

$$R_{sm} = \frac{1}{5}\sum_{i=1}^{5} s_{mi} \tag{9.19}$$

The mean peak spacing s_{mi} is the wavelength of the roughness profile that must contain at least one peak and one valley of the surface roughness.

Fig. 9.10 Mean peak spacing R_{sm}

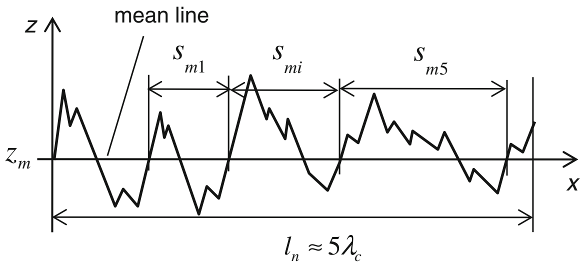

Fig. 9.11 Arithmetic mean roughness R_a

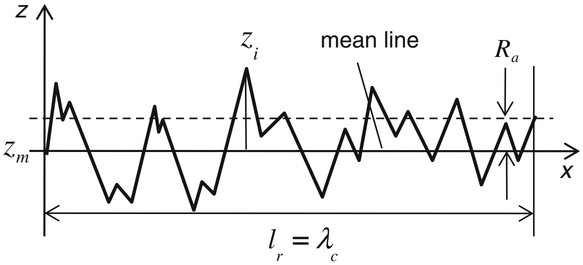

Fig. 9.12 Root mean square roughness R_q

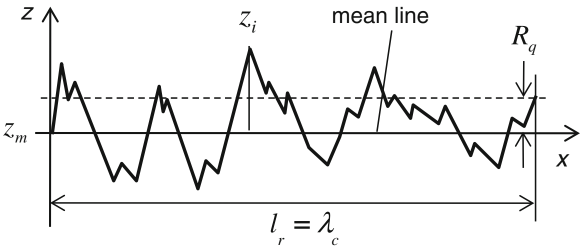

- *Mean roughness R_a* (DIN EN ISO 4287, ASME B46.1), see Fig. 9.11

It is the arithmetic average roughness of N roughness heights z_i. For the simplicity, the roughness height z_i is measured from the mean line within the sampling length l_r.

$$R_a \equiv \frac{1}{l_r} \int_0^{l_r} |z(x)| dx \approx \frac{1}{N} \sum_{i=1}^{N} |z_i| \tag{9.20}$$

- *Root mean square (rms) roughness R_q* (DIN EN ISO 4287, ASME B46.1), see Fig. 9.12

The rms roughness height of N points within the sampling length l_r is defined as where the peak and valley heights are considered.

$$R_q \equiv \sqrt{\frac{1}{l_r} \int_0^{l_r} z^2(x) dx} \approx \sqrt{\frac{1}{N} \sum_{i=1}^{N} z_i^2} \tag{9.21}$$

- *Mean roughness depth R_z and maximum roughness depth $R_{\max}$* (DIN EN ISO 4287, ASME B46.1).

The mean roughness depth R_z is the arithmetic average value of the five single roughness depths $R_{z,i}$ of five consecutive sampling lengths l_r within the evaluation length l_n.

$$R_z \equiv \frac{1}{5} \sum_{i=1}^{5} R_{z,i} \tag{9.22}$$

The maximum roughness depth $R_{\max}$ is the largest single roughness depth of the five roughness depths within the evaluation length l_n.

$$R_{\max} \equiv \max_{i=1,..,5} (R_{z,i}) \tag{9.23}$$

where $R_{z,i}$ and $R_{\max}$ are shown in Fig. 9.13.

- *Material ratio R_{mr}* (DIN EN ISO 4287, ASME B46.1)

The material ratio is the ratio of the sum $l(c)$ of all material lengths l_i at the surface height z to the total material length l_n. It is also called the *bearing length ratio* according to the ASME B46.1.

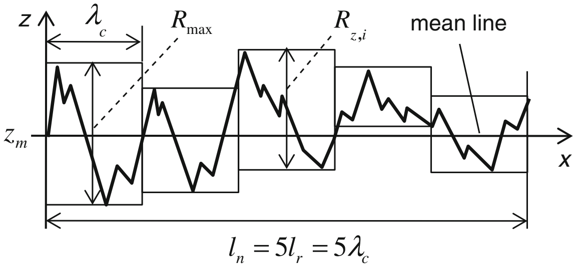

Fig. 9.13 Mean roughness depth R_z and maximum roughness depth $R_{\max}$

$$R_{mr}(z) \equiv \frac{\sum l_i(z)}{l_n} 100\,[\%] \tag{9.24}$$

- *Abbott-Firestone curve (Abbott curve)*

The Abbott-Firestone curve is the most important surface roughness parameter that is additionally used to evaluate the surface roughness quality. The Abbott curve evaluates the tribological surface roughness quality of the samples that have the same mean roughness R_a and R_z. In this case, the shape of the Abbott curve decides which surface roughness is better.

According to the ASME B46.1, the Abbott curve is also called the *bearing area curve* (BAC). In the statistical analysis, the Abbott curve is in fact the probability distribution function of the surface roughness height resulting from its distribution density function (see Appendix D). At first, the construction of the Abbott curve is derived from the profile of the roughness height $z(x)$. At the cutting line with the surface height z, the material ratio R_{mr} is computed from the sum of all cutting lengths l_i to the total length l_n, as shown in Fig. 9.14.

The new dimensionless surface height c is defined as

$$c \equiv \frac{z - \bar{z}}{\sigma} \tag{9.25}$$

where σ is the standard deviation of the roughness height in Eq. (9.15).

The dimensionless surface height c versus the material ratio R_{mr} is plotted on the RHS of Fig. 9.14. The bell-shaped curve is called the *Abbott-Firestone curve*. Obviously, the material ratio equals 0 % at the maximum peak because no peak is cut; the material ratio arrives at 100 % at the minimum valley since all cutting lengths equal the total length. However, in practice, one moves the ordinate surface height c from the initial position of R_{mr} = 0–5 % (experience value) in the direction of the abscissa material ratio R_{mr}. Therefore, it makes sure that the reference line c_{ref} lies at the highest peak of the surface height because of initial wears after a short operating period.

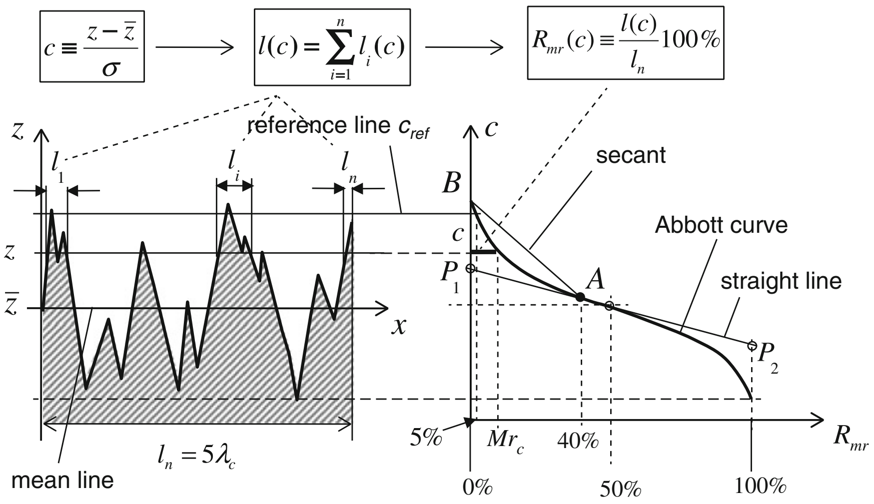

Fig. 9.14 Abbott curve and the material ratio R_{mr}

In another way, the Abbott curve can be derived using the amplitude density function (ADF) $p(c)$ of the surface roughness profile, as shown in Fig. 9.15 [2].

The ADF $p(c)$ is the number of surface heights between the two cutting heights z and $z + dz$. The cumulative distribution function $P(c)$ of the ADF $p(c)$ of the surface roughness height is in fact the material ratio at the dimensionless surface height c (see Appendix D).

$$P(c) = \int_{c}^{\infty} p(c)dc \equiv R_{mr}(c) \tag{9.26}$$

Thus,

R_{mr} ($c_{\max}$) = $P(c_{\max})$ ≈ 0 % at the highest peak of the surface height;
R_{mr} (0) = $P(0)$ ≈ 50 % at the mean line (c = 0);
$\mathrm{R_{mr}}$ ($c_{\min}$) = $P(c_{\min})$ ≈ 100 % at the lowest valley of the surface height.

- *Roughness R_{pk}, R_k, R_{vk}* (DIN EN ISO 13565-1 and -2)

R_{pk} is the reduced peak height in the Abbott curve in Fig. 9.16 that indicates the peak roughness of the surface; R_k is the core roughness depth indicating the plateau shape of the roughness surface; R_{vk} is the reduced valley height of the surface indicating the oil reservoir in the roughness surface.

The material ratios Mr_1 and Mr_2 are the smallest and largest material ratios at R_{pk} and R_{vk}, respectively. Both material ratios determine the shape of the Abbott curve that indicates the important tribological parameter besides the mean roughness R_a and mean roughness depth R_z.

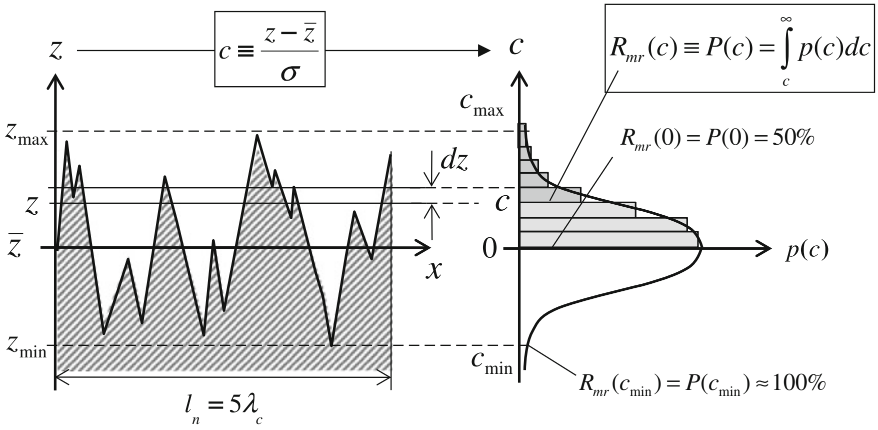

Fig. 9.15 Amplitude density function (ADF) of the surface roughness profile

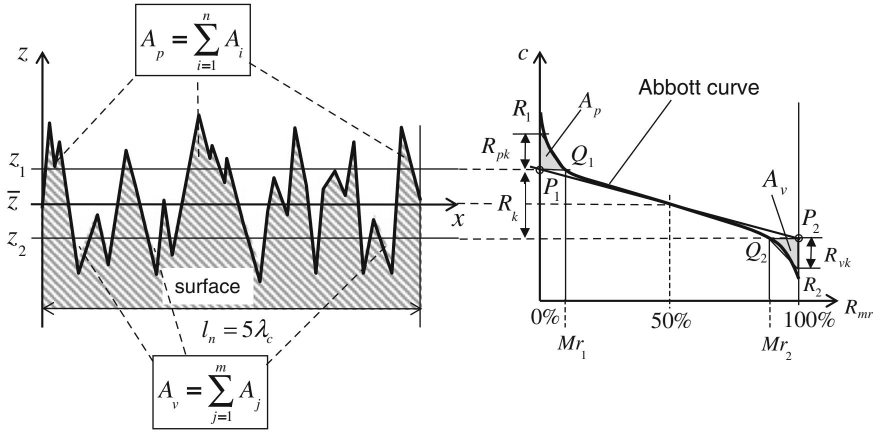

Fig. 9.16 Roughness R_{pk}, R_k, R_{vk} and material ratios Mr_1 and Mr_2

In the following section, the roughness R_{pk}, R_k, and R_{vk} and the material ratios Mr_1 and Mr_2 are determined in the Abbott curve in Figs. 9.14 and 9.16. At first, we create the secant *AB* with R_{mr} (*A*) of 40 % in Fig. 9.14. Then, we rotate the secant *AB* about point *A* until it is tangential to the left half-branch of the Abbott curve at the point *A*. The prolonged secant, called the straight line P_1AP_2, cuts the ordinates with R_{mr} = 0 and 100 % at P_1 and P_2, respectively, as plotted in Fig. 9.16. The corresponding surface heights z_1 and z_2 at P_1 and P_2 intersect the Abbott curve at Q_1 and Q_2, respectively. Therefore, the smallest and largest material ratios Mr_1 and Mr_2 are found at Q_1 and Q_2 (see Fig. 9.16).

The area A_p is the sum of all peak surfaces A_i above the cutting surface height z_1. In the Abbott curve, the triangle $P_1Q_1R_1$ is constructed so that its area equals A_p. The altitude P_1R_1 is defined by the reduced peak height R_{pk}. Similarly, the reduced valley height R_{vk} is equal to P_2R_2 that is derived from the triangle $P_2Q_2R_2$ whose area equals A_v of the total groove area below the cutting surface height z_2. Finally, the core roughness depth R_k is the surface roughness height of P_1P_2, as shown in Fig. 9.16.

The reduced peak and valley heights are calculated as

$$R_{pk} = \frac{2A_p}{l_n Mr_1} \times 100\,\% \tag{9.27}$$

$$R_{vk} = \frac{2A_v}{l_n(100 - Mr_2)} \times 100\,\% \tag{9.28}$$

Generally, the core roughness depth R_k ($< \sim 1$–2 μm) should be small in the bearings to increase the bearing load capability because the bearing surface has less plateau shape. Note that the smaller the reduced peak height R_{pk} ($< \sim 0.5$–1 μm) is, the better the surface quality becomes. On the contrary, the reduced valley height R_{vk} ($< \sim 1$–2 μm) should be larger than R_{pk} to maintain the reserved lubricating oil in the valley grooves. Hence, the bearing is well lubricated at the start-stop driving cycle.

Figure 9.17 shows an example of two surface roughness heights that have the same R_a but different roughness values of R_{pk}, R_k, and R_{vk}. Obviously, the first one has only a moderate tribological surface characteristic due to the higher value of $R_{pk,1}$ compared to $R_{pk,2}$ that could cause wear in the surface. On the contrary, the latter with smaller values of $R_{k,2}$ and $R_{pk,2}$ is tribological better because the surface has less plateau and the peaks of the surface roughness are reduced; its $R_{vk,2}$ is higher than the first one. Hence, the surface has more oil reservoir to lubricate the bearing surface.

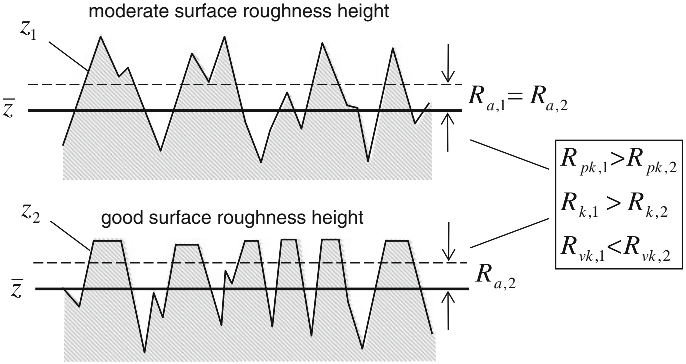

Fig. 9.17 Comparison of two surface roughness heights

Figure 9.18 shows three surface roughness heights that are finished by different methods of honing, eroding, and turning. Despite the nearly same roughness R_a and $R_{\max}$, they have different qualities of tribological surface characteristics. The honed surface is the best because all peak heights were removed and the groove depths are large enough to maintain sufficiently reserved oil for lubrication. The eroded surface has a moderate quality since many peaks remain and thus could cause wears at the asperities and reduces the bearing load capability. The turning surface with the largest R_z is the worst since it has many peaks with the largest reduced peak height R_{pk} due to the turning profile. It causes reduction of the bearing load capability and therefore induces the bearing friction due to abrasive wear at the peaks (asperities). In this case, we have to consider the other roughness parameters of R_{pk}, R_k, R_{vk}, and R_{mr}.

Besides the surface roughness depths R_z and R_a, the Abbott curve is additionally used to analyze the surface roughness quality. Generally, good tribological surface roughness characteristics are possibly smallest reduced peak heights R_{pk} and possibly largest reduced valley heights R_{vk}.

The Abbott curve is derived from the measured values of the surface roughness height with the lowest and largest material ratios of Mr_1 and Mr_2 according to Eqs. (9.27 and 9.28), as shown in Fig. 9.19.

They determine the shape of the Abbott curve of the roughness surface height. By experience, at the same roughness R_a or R_z, the Abbott curve with a *convex shape* indicates the best tribological quality of the surface roughness height (case *c*). Therefore, the best surface roughness characteristic is the third case with the small reduced peak heights R_{pk} (low peak surface roughness), the high reduced valley heights R_{vk} (more oil reservoir), and the small core roughness depth R_k with less plateau of the surface roughness. On the contrary, the surface with a *concave shape*

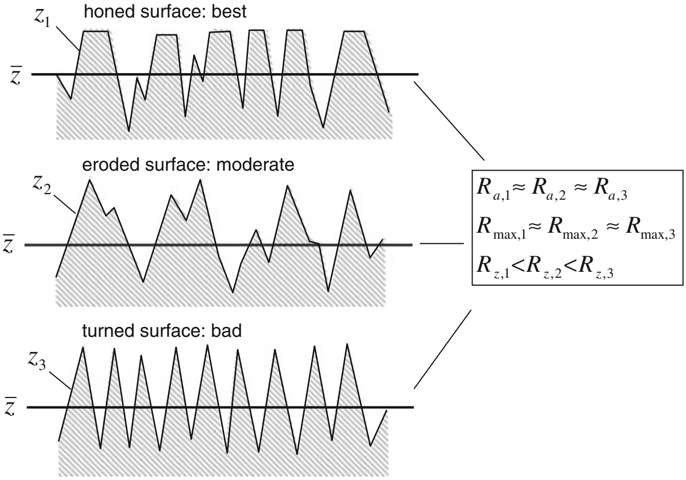

Fig. 9.18 Roughness heights at different finishing methods

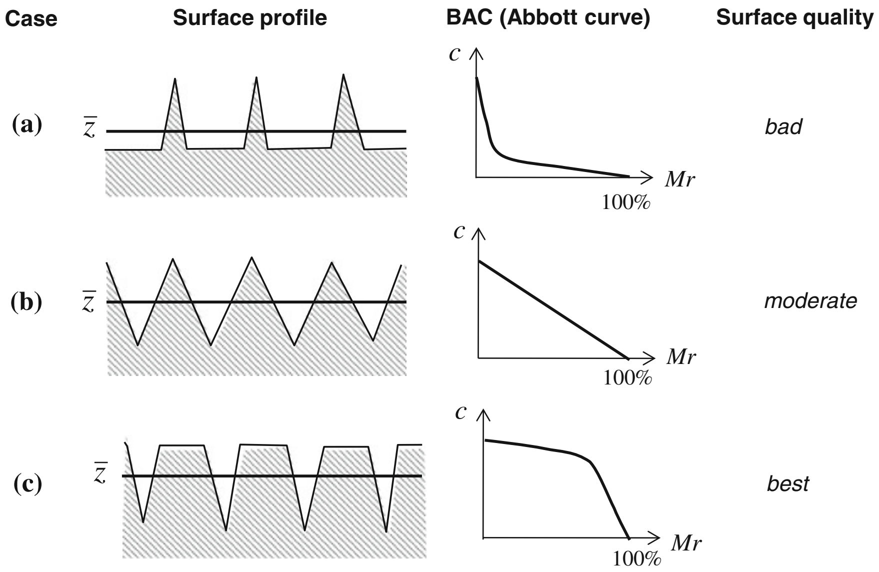

Fig. 9.19 Analysis of surface quality using Abbott curves

shows the bad tribological surface roughness quality (case *a*). They have many sharp asperities with the large reduced peak heights R_{pk} (high peak surface roughness) and the low reduced valley heights R_{vk} (less oil reservoir). The Abbott curve of the case *b* has a *linear shape* that is considered as moderate.

9.7 Elastic and Plastic Deformations in the Bearings

To study the wear mechanism in the bearings, some backgrounds of the elastic and plastic deformations of material are required [3, 5].

First, a small load acts upon the material that begins deforming; as soon as the load is removed, its form returns to the initial condition. This deformation is defined as *elastic deformation*. On the contrary, in case of *plastic deformation*, a heavy load acts upon the material. As a result, the resulting stress in the material exceeds the yield stress σ_o, the deformed material remains and does not return to the initial condition although the acting load is removed from it (see Fig. 9.20).

At further increasing the acting load at the plastic deformation, the material suddenly breaks up (material fracture) shortly after the ultimate tensile stress σ_u. Therefore, the wear process begins with the loss of the surface asperities (roughness peaks) that abrade the moving surfaces and cause wear paths on the surfaces.

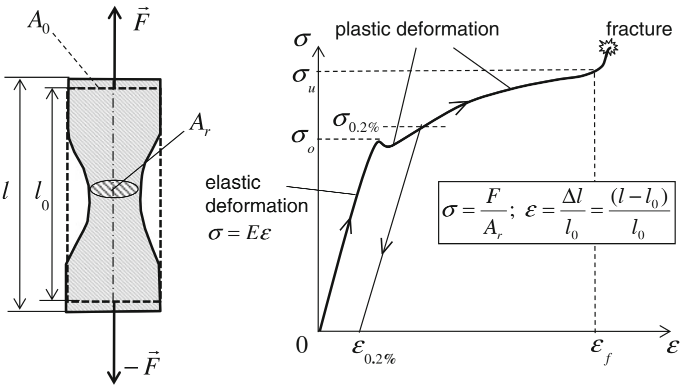

Fig. 9.20 Stress-strain diagram of a ductile material

9.7.1 Normal Stress

Applying the tensile force F on a cylindrical specimen with the initial cross-sectional area A_0 and length l_0, the body begins deforming in the axial direction.

The normal stress σ is defined as the ratio of the acting force to the real cross-sectional area.

$$\sigma = \frac{F}{A_r} \tag{9.29}$$

In the elastic deformation, the stress is proportional to the strain according to the Hooke's law.

$$\sigma = E\left(\frac{l - l_0}{l_0}\right) = E\frac{\Delta l}{l_0} \equiv E\varepsilon \tag{9.30}$$

where

E is the elasticity modulus (Young's modulus);
ε is the normal strain defined as the relative change of the length from l_0 to $l > l_0$.

The Hooke's law is valid as long as the stress is less than the *yield stress* σ_o; i.e., the deformation is elastic and returns to the initial position when the acting load is removed. At further increasing the acting force, the normal stress increases larger than the yield stress σ_o; hence, the deformation of the body becomes plastic where the Hooke's law has been no longer valid. With a plastic stress of 0.2 %, the strain remains at $\varepsilon = 0.2$ % after removing the acting force. The deformation is plastic up to the *ultimate tensile stress* σ_u. After exceeding the ultimate tensile stress, the normal stress sharply increases in a very short time, and the material breaks up. Shortly before the fracture occurs, the real cross-sectional area A_r significantly reduces due to material contraction at a constant load F, as shown in Fig. 9.20. Therefore, the normal stress sharply increases before the material fracture happens according to Eq. (9.29).

9.7.2 Shear Stress

Applying the force F acting on a specimen in the tangential direction, the body form deforms at a shear strain t. The *shear rate* $\dot{\gamma}$ is defined as the ratio of the shear strain t to the specimen height h (see Fig. 9.21).

The *shear stress* is written at the contact surface A as

$$\tau = \frac{F}{A} = G\left(\frac{t}{h}\right) \approx G\dot{\gamma} \tag{9.31}$$

where G is the *shear modulus* of the material.

The shear modulus is calculated from the *elasticity modulus* E and the *Poisson ratio* v as

$$E = 2G(1 + v) \tag{9.32}$$

where v equals 0.25–0.30 for most metals. Thus,

$$G = \frac{E}{2(1 + v)} \approx (0.385\ldots0.400)E \tag{9.33}$$

The elasticity modulus E can be used for

- low-alloy steels: $E \approx 212$ GPa;
- tool steels (highly alloyed steels): $E \approx 230$ GPa;
- brass, copper alloys, and bronze: $E \approx 96$ to 114 GPa.

Fig. 9.21 Shear stress and shear rate in a testing specimen

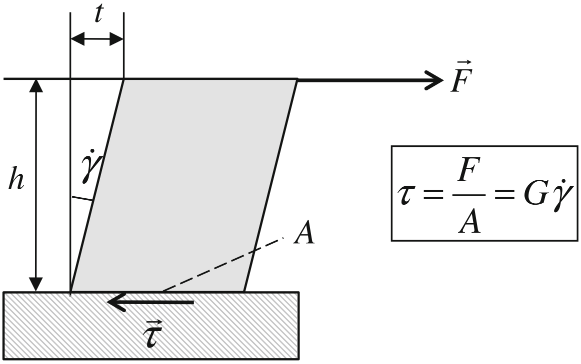

9.7.3 Friction Force in the Bearings

The rotor unbalance induces the normal load F_n acting on the bearing surface. At the contact zone between the journal and bearing, the friction force F_t occurs on the journal surface opposite to the rotational direction of the rotor. The friction force is proportional to the normal load with a friction coefficient. Figure 9.22 shows the normal load and the friction force in the bearing. In fact, the adhesion and abrasion frictions between the bearing and journal induce the total friction force.

$$\begin{aligned} F_t &= \mu_f F_n \\ &= F_{\text{adh}} + F_{\text{abr}} = (\mu_{\text{adh}} + \mu_{\text{abr}})F_n \end{aligned} \tag{9.34}$$

The total friction coefficient results from the adhesive and abrasive friction coefficients as

$$\mu_f = \mu_{\text{adh}} + \mu_{\text{abr}} \tag{9.35}$$

The adhesive friction force results from the shear stress and real contact area as

$$F_{\text{adh}} = \tau A_r \tag{9.36}$$

within the real contact area A_r is determined as the ratio of the normal load to the hardness H of the softer material at the plastic deformation.

$$A_r = \frac{F_n}{H} \tag{9.37}$$

The hardness of material H is the mean contact pressure that results from the normal load and permanent indentation at the plastic deformation as

$$H \equiv p_{\text{mean}} = \frac{F_n}{A_r} \tag{9.38}$$

The plastic deformation begins with $p_{\text{mean}} \approx 1.07\text{–}1.1\sigma_o$ (σ_o = yield stress). At $p_{\text{mean}} \approx 3\sigma_{\text{o}}$, it fully develops in the permanent indentation. According to [5], the hardness H is nearly 2.8–3 times of the yield stress for intenders with spherical, conical, pyramid, and flat-end shaped geometries.

$$H \approx (2.8\ldots3)\sigma_o \tag{9.39}$$

Substituting Eqs. (9.36 and 9.37), one obtains the adhesive friction coefficient.

$$\mu_{\text{adh}} \equiv \frac{F_{\text{adh}}}{F_n} = \frac{\tau}{H} \tag{9.40}$$

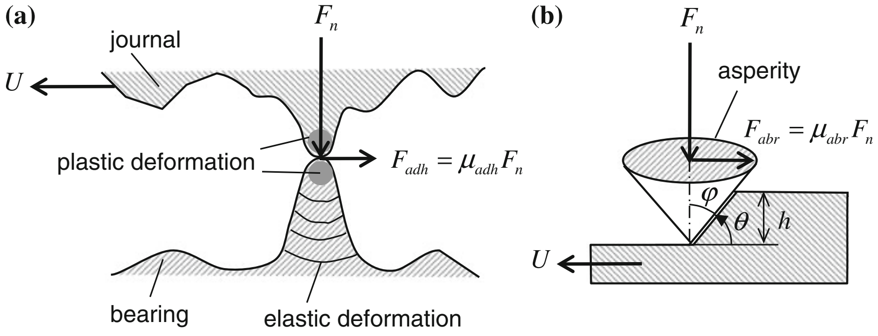

Fig. 9.22 Adhesive and abrasive friction forces in the bearing. **a** Adhesion friction. **b** Abrasion friction

According to [9], the abrasive friction coefficient is calculated as

$$\mu_{\text{abr}} = \frac{2}{\pi}\cot\varphi = \frac{2}{\pi}\tan\theta \tag{9.41}$$

where φ is the cone semi-angle of the asperity; θ is the abrasive angle of material (see Fig. 9.22).

Thus, the total friction coefficient results from Eqs. (9.35, 9.40, and 9.41).

$$\begin{aligned}\mu_f &= \mu_{\text{adh}} + \mu_{\text{abr}} \\ &= \frac{\tau}{H} + \frac{2}{\pi}\tan\theta\end{aligned} \tag{9.42}$$

Normally, the abrasive angle of most materials is less than 10°; hence, the abrasive friction coefficient is about 0.1. The adhesive friction coefficient is 0.17 to 0.2 for similar hardness of materials where the abrasive friction coefficient is negligible, and <0.3 for hard to softer materials. In fact, the total friction coefficient is quite larger than these theoretical values between 0.3 and 0.4.

The work hardening and junction growth in the contact zone is to blame for this discrepancy [9]. At the plastic deformation, the atomic dislocations are removed from the material grid structure. Therefore, the material becomes harder; the shear and yield stress, and the material hardness are strengthened. This process is called the *work hardening* during plastic deformation. Additionally, the real contact area increases at the plastic deformation, cf. Eq. (9.37). It is called the *junction growth* at the contact zone.

Straightforwardly, the plastic deformation occurs in the contact zone because the normal load and friction force concentrate on a very small contact area of the surface roughness asperities (high R_{pk} and R_z). The normal stress that is far away from the asperity is smaller than in the contact zone. Therefore, the elastic deformation occurs at far away from the contact zone (see Fig. 9.22). During plastic deformation at the contact zone, the shear stress increases faster than the hardness. As a result, the friction coefficient increases in the contact zone between the journal and the bearing. Therefore, the friction force increases in the plastic deformation due to the work hardening and junction growth, cf. Eqs. (9.34, 9.38, 9.40, and 9.42).

9.7.4 Friction Power in the Bearings

The following section deals with the friction power in the bearings that occurs in the boundary, mixed, and HLs in the Stribeck curve, as displayed in Fig. 9.7.

The friction power P_f in the bearings results from the friction force F_f and relative velocity U. It consists of the friction powers in the ML P_m and the HL P_h. At the large oil-film thickness $h \geq h_0$, the friction power in the HL P_h at $\varepsilon = 1$ dominates the bearing friction power. In other case $h \ll h_0$, the friction power in the boundary/ML P_m at $\varepsilon = 0$ is dominant in the bearing friction power at the small oil-film thickness.

Therefore, the bearing friction power can be expressed in terms of the hydrodynamic and mixed friction powers in the bearing.

$$\begin{aligned} P_f &= F_f U = (\tau \cdot A)U \\ &= (1-\varepsilon)P_m + \varepsilon P_h \\ &= [(1-\varepsilon)\mu_m + \varepsilon\mu_h]\sigma_N UA \end{aligned} \tag{9.43a}$$

where

ε is the weighting factor for the fully hydrodynamic ($\varepsilon = 1$) and ML ($\varepsilon = 0$);
μ_m is the friction coefficient in the ML;
μ_h is the friction coefficient in the HL;
σ_N is the normal stress on the bearing;
A is the bearing surface.

In case of a small bearing surface, the oil-film thickness reduces itself to increase the oil pressure in the bearing clearance against the bearing load. At further increasing the bearing load, the oil-film thickness becomes smaller than the oil-film thickness h_0 (see Fig. 9.23). Thus, the ML regime occurs in the bearing in which the friction coefficient μ_m significantly increases due to the adhesive and abrasive friction on the bearing surface. According to Eq. (9.43a), the mixed friction power P_m extremely increases much higher than the friction power P_h in the HL.

As a result, the effective friction power in the bearing increases drastically although the bearing surface is reduced. However, if we enlarge the bearing surface excessively, the oil-film thickness will increase in the fully HL regime. In this case, the hydrodynamic friction power P_h could also increase due to the large bearing

Fig. 9.23 Specific friction power in the bearing versus oil-film thickness

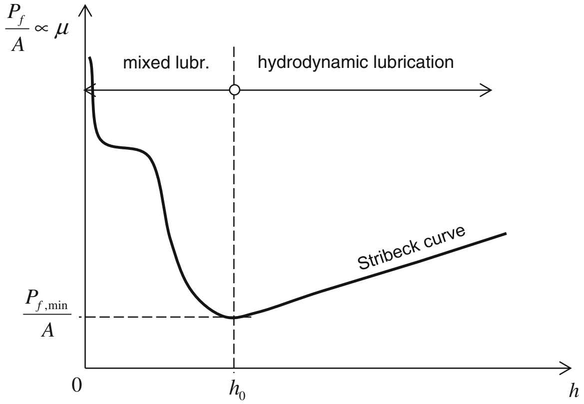

surface and high oil viscosity. Therefore, the effective bearing friction power also increases at enlarging the bearing surface in the fully HL. The friction power reaches a minimum value at the oil-film thickness h_0 from which the fully HL begins. The best way is to operate the bearing near the oil-film thickness h_0.

The specific friction power in the bearing is defined as

$$\begin{aligned}\frac{P_f}{A} &= [(1-\varepsilon)\mu_m + \varepsilon\mu_h]\sigma_N U \\ &\equiv \mu\sigma_N U \;\propto\; \mu\end{aligned} \tag{9.43b}$$

Figure 9.23 shows the behavior of the specific friction power of the bearing in the mixed and fully HL regimes in the Stribeck curve. The result indicates that the specific friction power strongly rises at $h \ll h_0$. Therefore, decreasing the bearing surface to reduce the bearing friction power is not always correct. In some cases, we obtain an increased friction power in the bearing due to the very large mixed friction coefficient μ_m.

The reduction of the bearing friction by moderately decreasing the bearing surface is correct when the operating condition is in the fully HL regime ($h > h_0$) with a smaller friction coefficient μ_h.

$$P_{f,h} = \mu_h\sigma_N UA$$

In the ML regime ($h \ll h_0$), the friction coefficient μ_m strongly increases leading to a high friction power in the bearing.

$$P_{f,m} = \mu_m\sigma_N UA \gg P_{f,h}$$

In this case, we must even enlarge the bearing surface or reduce the bearing load so that the oil-film thickness in the bearing increases to h_0.

9.7.5 Mohr's Circle Diagram

The normal force and bending moment caused by the friction force act upon the asperities of the bearing (see Fig. 9.24). The asperities begin deforming under the acting load and moment. At increasing external forces and moments, the plastic deformation occurs at the asperities. When the normal and shear stresses exceed their ultimate stresses, the asperities break up in the bearing clearance leading to abrasive wears.

In the following section, we compute the principle stresses using Mohr's circle method. The principle normal stresses result from solving the cubic stress equation of σ [3].

$$\begin{vmatrix} (\sigma_x - \sigma) & \tau_{xy} & \tau_{zx} \\ \tau_{xy} & (\sigma_y - \sigma) & \tau_{yz} \\ \tau_{zx} & \tau_{yz} & (\sigma_z - \sigma) \end{vmatrix} = 0 \tag{9.44}$$

In case of $\tau_{zx} = \tau_{yz} = 0$, and $\tau_{xy} \neq 0$ for simplicity, we have three solutions:

$$\sigma_1, \sigma_2 = \left(\frac{\sigma_x + \sigma_y}{2}\right) \pm \sqrt{\left(\frac{\sigma_x - \sigma_y}{2}\right)^2 + \tau_{xy}^2} \tag{9.45}$$

and

$$\sigma_3 = \sigma_z \tag{9.46}$$

The material failure takes place if the maximum tensile stress σ_1 in Eq. (9.45) due to bending moment exceeds the ultimate tensile stress σ_u, or the maximum shear stress $\tau_{\max}$ in Eq. (9.49) is larger than the critical shear stress τ_c.

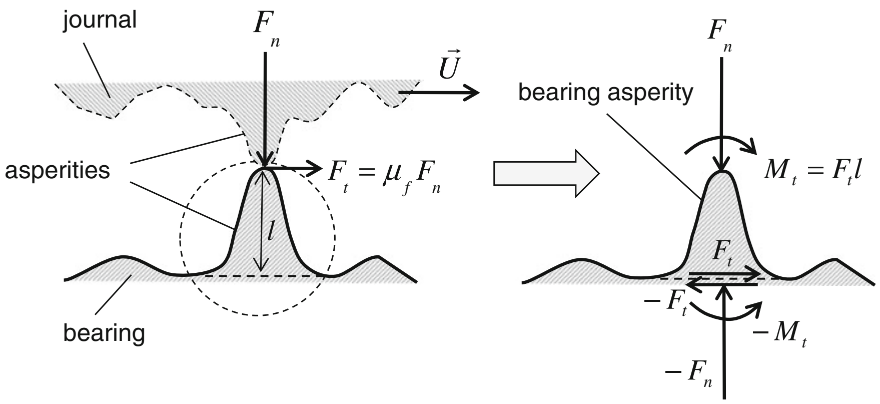

Fig. 9.24 Loads acting on the asperity of the bearing surfaces

In a three-dimensional case, all six components of normal and shear stresses in the directions of x, y, and z exist in the asperities. Using the coordinate transformation between the inertial coordinate system (x, y, z) and principle coordinate system (1, 2, 3), we obtain only the normal stresses σ_1, σ_2, and σ_3 in the directions 1, 2, and 3 in which the shear stresses τ_1, τ_2, and τ_3 equal zero.

Applying the Mohr's circle diagram, the related stresses in the principle coordinate system (1, 2, 3) are calculated graphically from the principle normal stresses σ_1, σ_2, and σ_3, as shown in Fig. 9.25.

The maximum principle shear stresses in the planes inclined 45° to the principle normal stress axes in the directions 1, 2, and 3 are calculated as

$$\tau_1 = \frac{|\sigma_2 - \sigma_3|}{2}; \quad \tau_2 = \frac{|\sigma_1 - \sigma_3|}{2}; \quad \tau_3 = \frac{|\sigma_1 - \sigma_2|}{2} \tag{9.47}$$

The normal stresses perpendicular to the principle shear stresses result as

$$\sigma_{\tau 1} = \frac{\sigma_2 + \sigma_3}{2}; \quad \sigma_{\tau 2} = \frac{\sigma_1 + \sigma_3}{2}; \quad \sigma_{\tau 3} = \frac{\sigma_1 + \sigma_2}{2} \tag{9.48}$$

The maximal shear stress for any plane in the asperity is the largest shear stress of the principle shear stresses from Eq. (9.47).

$$\tau_{\max} = \max(\tau_1, \tau_2, \tau_3) \tag{9.49}$$

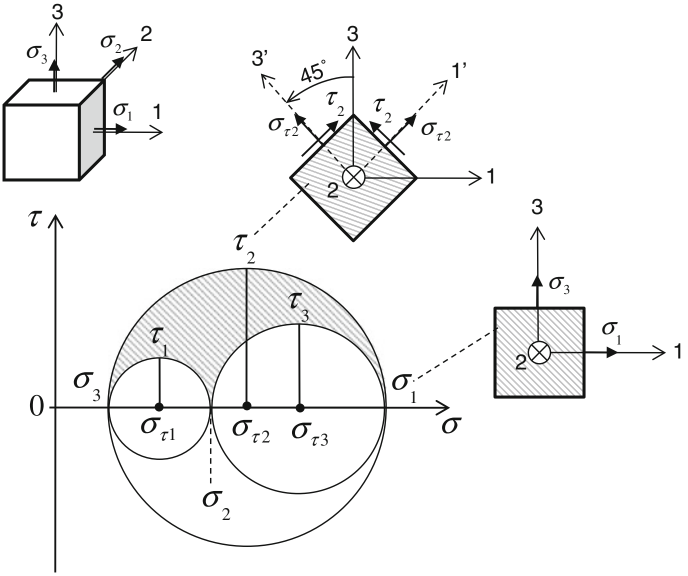

Fig. 9.25 Calculation of principle stresses using Mohr's circle diagram

All states of stress (σ, τ) in the asperities occur in the shaded area, which lies in the upper half plane outside the two small circles and inside the large one displayed in the Mohr's circle diagram in Fig. 9.25.

9.8 Wear Mechanisms in the Oil-Film Bearings

Oil-film bearings work on the hydrodynamic principle in the various lubrication regimes, such as fully hydrodynamic, mixed, and BLs in the Stribeck curve (see Fig. 9.7).

Theoretically, wear in the bearing does not occur or is negligibly small in the fully HL because the oil film is thick enough to prevent wear in the bearing. In case of clean oils, only the hydrodynamic friction occurs in the oil film, as discussed in Sect. 9.3. However, contaminated oil with hard particles causes wear in the bearing due to the adhesion and abrasion forces between the bearing and journal.

If the oil-film thickness is smaller than the limit oil-film thickness, the mixed and BLs occur in the bearing clearance. The asperities of the bearing and journal surfaces slide to each other leading to the plastic deformation due to thermomechanical loads acting on the asperities. As a result, it causes at first the *adhesive wear* at the asperities due to plastic shearing, then losses the material because their asperities break up. In the abrasive wear, the hard particles in the contaminated oil, broken bits of the asperities, and still remaining asperities of the surfaces abrade the surface of the softer material. Therefore, the material is removed from the bearing surface with time leading to wear. In the mixed and partial BLs, the wear process in the bearing begins with the adhesive friction at the asperities of the roughness surfaces. Wears continue further by loss of the asperities, and it is eventually intensified by the abrasive wear of the hard particles in the BL leading to seizure and damage of the bearing.

Figure 9.26 shows the adhesive wear mechanism where the asperities in the softer material bearing (brass) contact the other asperities of the moving journal of

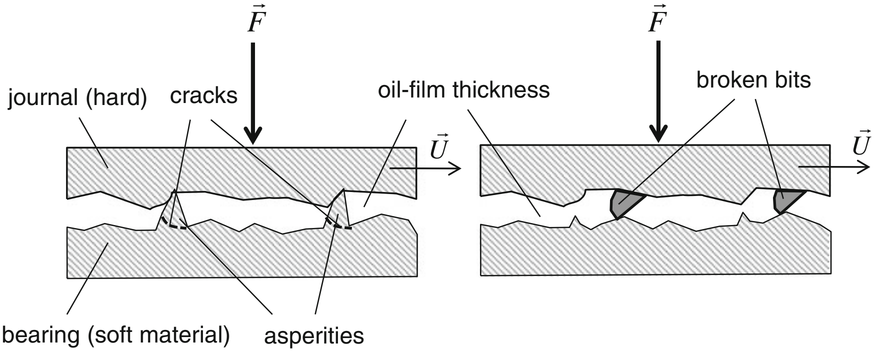

Fig. 9.26 Adhesive and abrasive wear in the bearing clearance

hard materials (highly alloyed steels) under the unbalance force and bending moment that act upon the bearing asperities with the relative circumferential velocity U of the journal to the bearing.

According to the deformation mechanism, as shown in Fig. 9.24, the asperities of the bearing surface begin deforming plastically under the acting loads. When the tensile and shear stresses in the asperities exceed the ultimate tensile and critical shear stresses, some asperities of the bearing and journal break off. Then, the broken bits together with the hard particles in lubricating oil cause the abrasive wear in the bearing.

The theoretical critical shear stress of a perfect material without any atomic dislocations in the material grid structure is given in [3] and [9].

$$\begin{aligned}\tau_{c,th} &= \frac{Gb}{2\pi h} \\ &\approx \frac{G}{10} \approx 10^2 \sigma_o\end{aligned} \tag{9.50}$$

where

G is the shear modulus;

b, h are the distance between the atoms in horizontal and vertical direction with ($b/h \sim 0.5$–1);

σ_o is the yield stress of material.

However, the real critical shear stress in an imperfect pure metal can be reduced by a factor of 300–10,000 of its theoretical value.

The theoretical tensile stress to break chemical bonds between the atoms in a perfect metal grid is estimated at

$$\sigma_{u,th} \approx \frac{E}{10} \tag{9.51}$$

where E is the elasticity modulus of material, see Eq. (9.33).

In fact, the real ultimate tensile stress of the common metals could be lower than the theoretical value by a factor of 10 to 100.

The contact types of wears are normally classified into *sliding, rolling, erosive, fretting,* and *slurry wear* [1].

Lubricating contaminated oil with hard particles supplies the two-oil-film bearing. The hard particles enter the bearing convergent wedge due to the wedge-velocity effect of the rotating journal and cause abrasive wear in the bearing that is classified into three different types of wears A, B, and C (see Figs. 9.27, 9.28 and 9.31).

- *Sliding wear* occurs when the hard and soft surfaces move relative to each other; the hard asperities slide over the soft surface. Hence, the soft material is removed due to plastic deformation and fracture of asperities.

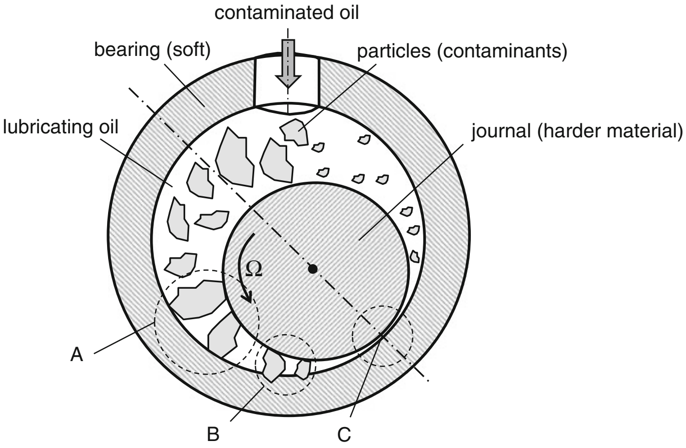

Fig. 9.27 Abrasive wear mechanism in a radial bearing

Fig. 9.28 Wear paths in a rotating floating ring bearing (RFRB)

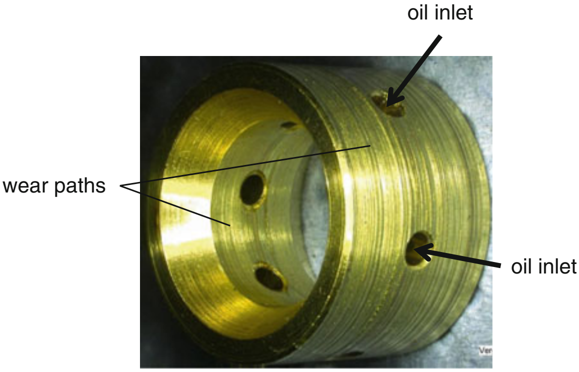

- R*olling wear* happens when the hard particles floating in lubricating oil roll over two moving surfaces in the small gap, such as the convergent clearance of the radial bearing and axial clearance of the thrust bearing (see Figs. 9.27, 9.28 and 9.29, 9.21). The asperities of the surfaces break up and cause abrasive wear on their surfaces in the rotating direction.
- *Erosive wear* is induced by the impact of the particles in lubricating oil or hard asperities against the surface. The impact kinetic energy of the hard particles and moving broken asperities deforms the asperities at the contact zones and causes material fracture when the tensile and shear stresses exceed the ultimate and critical values.
- *Fretting wear* is caused by the repeated cyclical microvibration of two contact surfaces under load, especially at a still stand. Due to the periodic rubbing, the bonding force between the atoms is weakened after repeating many vibration

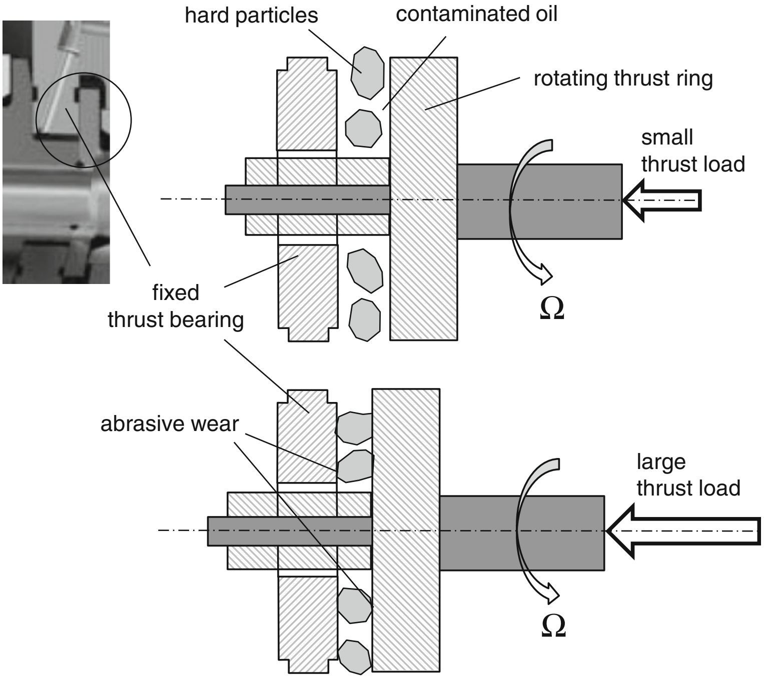

Fig. 9.29 Abrasive wear mechanism in a thrust bearing

cycles over a long operating time. As a result, adhesive wear occurs on the surfaces and is called the fretting wear (*false Brinelling*).

- *Slurry wear* occurs when the abrasive particles in lubricating oil float in the bearing clearance and abrade the asperities and surface of the bearing.

Figures 9.27, 9.28, 9.29 and 9.30 show the most typical types of the abrasive wear occurring in the radial and thrust oil bearings of the automotive turbochargers.

Figures 9.29 and 9.30 describe the wear mechanism in the thrust bearing. The oil-film thickness between the bearing and thrust ring becomes large at a small thrust load; hence, the hard particles in lubricating oil enter the active bearing clearance that is between the bearing and thrust ring. At increasing thrust load, the oil-film thickness decreases to the minimum of the axial clearance. The large thrust load induces the friction force between the particles and surfaces; the friction force causes abrasive wear on the surfaces between the bearing and thrust ring, especially in the soft bearing surface. Finally, abrasive wear leaves deep wear grooves on the bearing and disk surfaces. The wear grooves do not cause the failure of the bearing at once. However, the bearing damage could happen if the abrasive wear is continuously fortified leading to the mixed and BLs in the bearing.

Fig. 9.30 Wear paths on the surface of a thrust bearing

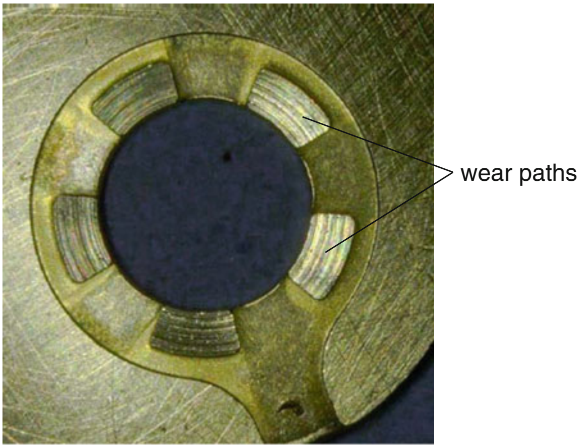

The abrasive wear is classified into three different types A, B, and C according to [9], as shown in Fig. 9.31 at which the journal material of highly alloyed steels is much harder than the bearing material of brass.

- Type A called the *three-body abrasive wear* shows the hard particles slide and roll on the bearing and journal surfaces, touch the asperities, deform them plastically, and finally remove them from the bearing surface.
- Type B called the *two-body abrasive wear* shows the hard particles and broken bits of the asperities are embedded in the softer bearing surface. Due to rotation, they abrade the journal surface as if a sand paper slides on it at a high speed. To prevent the journal from the abrasive wear, its surface is treated by nitriding. Nitriding is a heat-treating process of diffusing nitrogen (N_2) into the surface to create a hard coating layer on the surface, such as boron nitride (BN), titanium nitride (TiN), and silicon nitride (Si_3N_4).
- Type C called the *surface abrasive wear* shows the hard asperities of the journal surface abrade the softer bearing surface in case of poorly lubricated oil film in the partly and BLs. It mostly occurs at the minimum oil-film thickness in the bearing clearance, as displayed in Figs. 9.27, 9.28, 9.29, 9.30, and 9.31. The abrasive wear leaves wear paths on the bearing surface.

In the point of view of the tribological mechanism of wears, *fatigue and corrosive wears* should be taken into account besides the adhesive and abrasive wears (see Fig. 9.32).

- *Fatigue wear* is generated by the repeated cyclical friction between two moving surfaces after a certain number of rubbing cycles. It is caused by the fatigue fracture where the yield stress of material strongly reduces at increasing the number of rubbing cycles according to the Wöhler curve. There are two kinds of fatigue wear, the high-cycle fatigue wear (HCFW) occurs after a high number of rubbing cycles; the low-cycle fatigue wear (LCFW), after a low number of rubbing cycles.

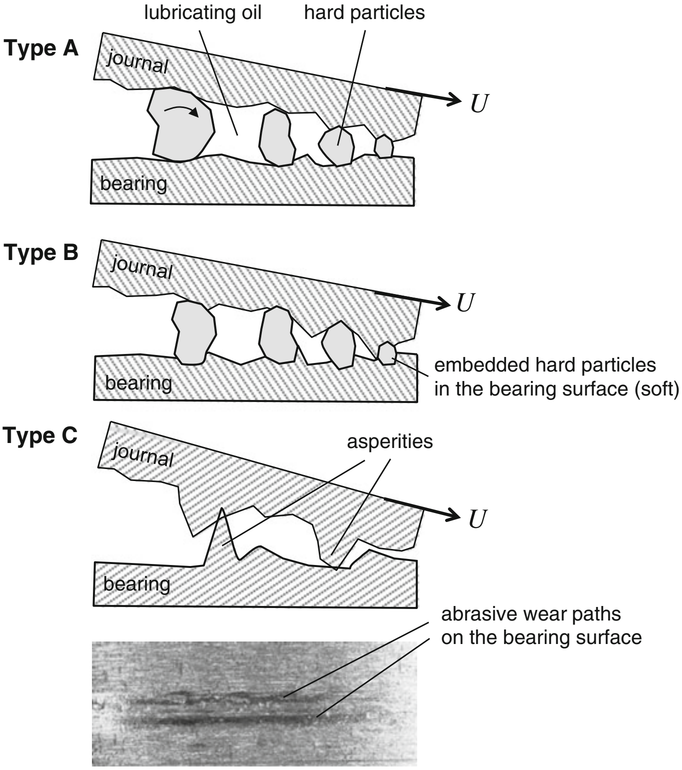

Fig. 9.31 Types of abrasive wear in the convergent wedge of a radial bearing

- *Corrosive wear* happens when the materials of the surfaces contact a corrosive substance (liquid or gas), such as dissolved water, fuel, and diffused air in lubricating oil that induces some tribochemical reactions (chemical and electrochemical) on the surfaces of the journal and bearing. Therefore, the materials of the surfaces are removed by the tribochemical corrosion.

In case of the ball bearings, two most failures of flaking (spalling) and false Brinelling due to contact fatigue often occurs after a long operating time. Both mechanisms reduce the lifetime of the bearing and cause the total failure of the machine.

The flaking-related failure occurs on the ball/races and generates the formation of large and deep cavities by a heavy load at the contact surface between the ball and races of a ball bearing. It induces intensive noises (NVH) and drastically reduces the lifetime of the bearing leading to a total failure in a few hundred km after noises occur.

Two root causes for the flaking failure are the *subsurface initial* and *surface initial microcracks* on the ball and race surfaces.

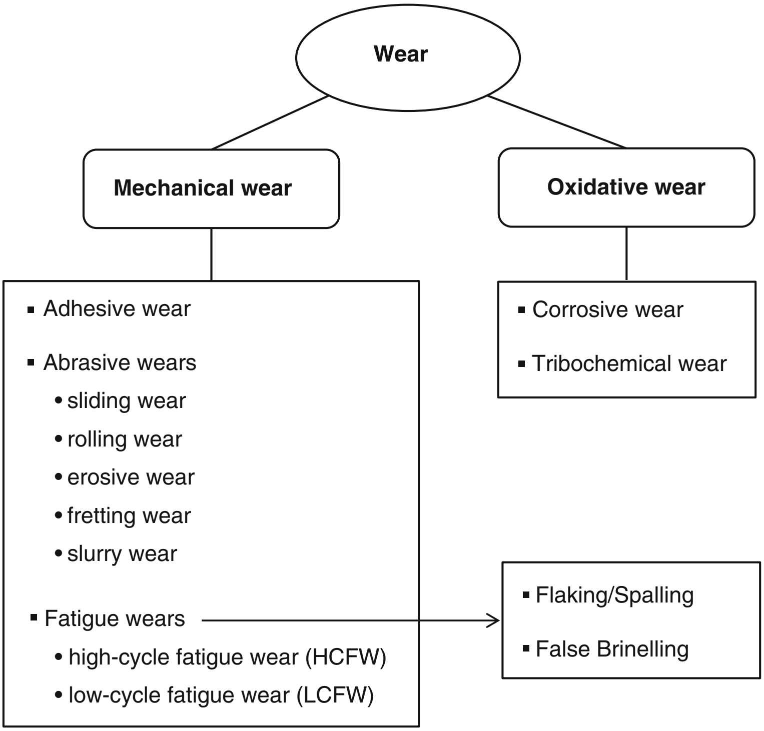

Fig. 9.32 Classification of wear mechanisms

First, the initial subsurface microcracks occurring about 100–150 μm under the surface are developed into the macrocracks that are caused by the high Hertzian stress at the contact surface in many repeated cyclical driving cycles. The developed subsurface macrocracks prolong in the upward direction to the surface. Due to contact fatigue, they lead to the material break up at the contact surface between the ball and races.

Second, the initial surface microcracks are induced on the surface due to the break up of the asperities of the surface at the small oil film thickness in the mixed/BL (see Fig. 9.7). Then, due to the elasto-hydrodynamic (EHD) effect, the microcracks turn into the macrocracks in the rotating direction of the ball. Further development of the macrocracks continues by the high shear stress of the oil film acting upon the surface in the repeated cyclical driving cycles. As a result, the developed macrocracks cause the material break up of the surface that is called flaking or spalling, as shown in Fig. 9.33. Note that the smaller the oil-film thickness is, the higher the shear stress acts upon the surface leading to the surface distress at the dimensionless oil-film thickness λ less than 3.

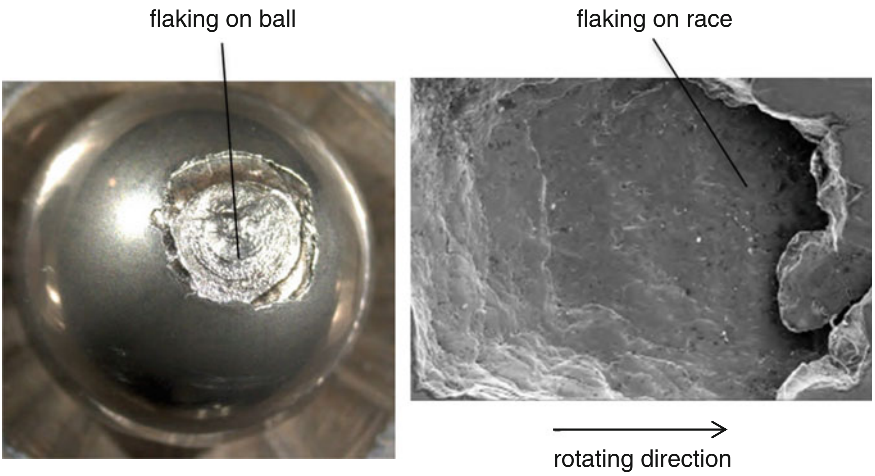

Fig. 9.33 Flaking in a ball bearing

Figure 9.34 shows the *false-Brinelling* (fretting mark) failure occurring in a ball bearing. False Brinelling is caused by high-frequency microvibrations in the axial direction of the bearing at the contact surfaces between the balls and races. It occurs at the transport or idle operating conditions under the bearing load, such as the rotor weight or radial preload of the bearing. In practice, it is known that false Brinelling has two negative effects of inducing bearing noises (NVH) and reducing the life-time of the bearing. In order to prevent the false-Brinelling-related failures, the bearing should be preloaded in the axial direction with an available thrust load using a flat spring (wave washer).

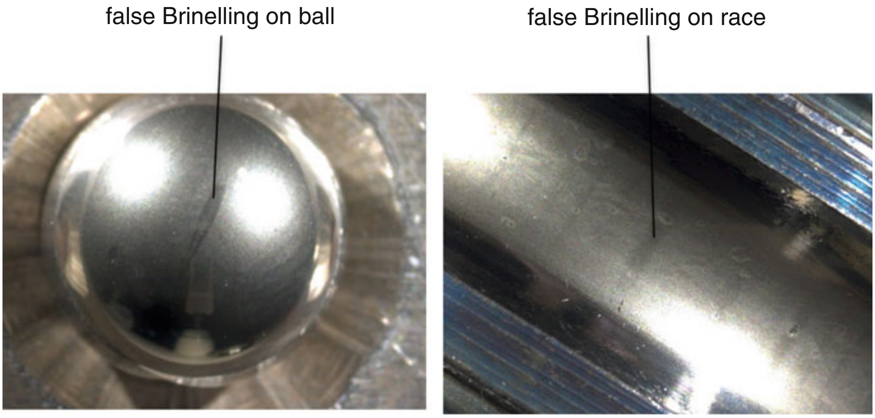

Fig. 9.34 False Brinelling in a ball bearing

Adhesive, abrasive, and fatigue wears are followed by the plastic deformation and fracture of materials; hence, they are called “mechanical wear”. On the contrary, the corrosive wear is caused by tribochemical reactions of corrosive mediums; therefore, it is called “oxidative wear”.

In practice, used and old lubricating oils after a long operating time in the automotive turbochargers contain about 5 % volumetric dissolved water and approximately 10 % volumetric dissolved fuel besides contaminated hard particles. In this case, the contaminated used oil is very thin and looses the necessary viscosity for the bearing lubrication. Under heavy loads, the oil-film thickness in the bearings becomes small and breaks up leading to the bearing wear and failure. Therefore, to prevent wears in the bearings, both lubricating oil and oil filter must be regularly changed in every period of 12–18 months at an average driving rate of 10,000 km/year according to the norm ISO 4406-1999: 24/23/18.

References

1. Bhushan, B.: Modern Tribology Handbook—Two-Volume Set. CRC Press Inc, Boca Raton (2000)
2. Bhushan, B.: Introduction to Tribology. Wiley, New York (2002)
3. Dowling, N.E.: Mechanical Behavior of Materials, 3rd edn. Pearson-Prentice Hall (2007)
4. Hamrock, B., Schmid, S.R., Jacobson, B.O.: Fundamentals of Fluid Film Lubrication, 2nd edn. Marcel Dekker Inc, New York (2004)
5. Johnson, K.L.: Contact Mechanics. Cambridge University Press, Cambridge (1985)
6. Kennedy F.E., et al.: Tribology, Lubrication, and Bearing Design—The CRC Handbook of Mechanical Engineers. CRC Press, Boca Raton (1988)
7. Khonsari, M., Booser, E.: Applied Tribology and Bearing Design and Lubrication, 2nd edn. Wiley, New York (2008)
8. Mahr: Surface Texture Parameters. Mahr GmbH, Germany (1999)
9. Mate, C.M.: Tribology on the Small Scale. Oxford University Press, Oxford (2008)